

A dynamical model of high-latitude convection derived from SuperDARN plasma drift measurements

E. D. P. Cousins¹ and S. G. Shepherd¹

Received 18 August 2010; revised 23 September 2010; accepted 7 October 2010; published 21 December 2010.

[1] A discrete set of climatological patterns of high-latitude ionospheric convection are derived using line-of-sight plasma drift data from the Super Dual Auroral Radar Network (SuperDARN). The patterns are derived independently for the Northern Hemisphere and Southern Hemisphere and for varying solar wind, interplanetary magnetic field (IMF), and dipole tilt angle conditions. By interpolating between discrete patterns, a dynamical model of convection is obtained, which can uniquely specify the high-latitude electrostatic potential distribution for a wide range of solar wind, IMF, and dipole tilt parameter values. Accounting for solar wind velocity dependencies in convection leads to better resolving the large-scale convection pattern, as compared to previous statistical models based on SuperDARN data. It is shown that the mesoscale features of the climatological model compare favorably to the features seen in instantaneous patterns of convection observed with SuperDARN. Comparison of the model to other statistical or empirical models derived from ground- and space-based measurements shows good agreement with most models.

Citation: Cousins, E. D. P., and S. G. Shepherd (2010), A dynamical model of high-latitude convection derived from SuperDARN plasma drift measurements, *J. Geophys. Res.*, 115, A12329, doi:10.1029/2010JA016017.

1. Introduction

[2] In the Earth's high-latitude ionosphere, circulation of plasma is primarily driven by interactions between the interplanetary magnetic field (IMF) carried in the solar wind and the Earth's magnetosphere. Knowing the instantaneous global distribution of plasma circulation (the convection pattern) is of interest because it is an indicator of the state of the coupled magnetosphere-ionosphere (M-I) system. A complete specification of the convection pattern is also useful for putting other smaller-scale measurements in context and for modeling layers of the atmosphere below, as it serves as an energy input at the top boundary.

[3] A variety of ground- and space-based instruments are currently used to measure the convection of plasma in the ionosphere. However, these instruments often do not have sufficient spatial coverage to define the complete pattern of convection. In these cases, an empirical model of high-latitude convection must be used in place of, or to supplement, instantaneous measurements. Theoretical considerations of the driving mechanisms of convection as well as previous empirical studies [e.g., *Dungey*, 1961; *Cowley*, 1982; *Reiff et al.*, 1981; *Wygant et al.*, 1983; *Reiff and Burch*, 1985; *Cowley and Lockwood*, 1992; *Ruohoniemi et al.*, 2002; *Lester et al.*, 2006] have led to the use of the IMF clock angle, the IMF transverse magnitude, the solar

wind velocity, the geographic season or dipole tilt, and sometimes the solar wind density, as typical organizing parameters for such models.

[4] In past studies, models of high-latitude convection have been derived using data from low-altitude satellites [e.g., *Heppner and Maynard*, 1987; *Lu et al.*, 1989; *Weimer*, 1995, 1996, 2001, 2005; *Papitashvili et al.*, 1994, 1999], from ground-based incoherent backscatter radars [*Foster et al.*, 1986; *Holt et al.*, 1987; *Zhang et al.*, 2007] and coherent backscatter radars [*Ruohoniemi and Greenwald*, 1996, 2005; *Pettigrew et al.*, 2010]. Most of these models are presented as discrete, average patterns of convection that are valid for specific ranges of interplanetary and sometimes geographic parameters. The models of *Weimer* [1996, 2001, 2005], on the other hand, were presented as dynamical models which produce a convection pattern for any specified driving condition.

[5] A discrete set of statistical convection patterns was obtained by *Pettigrew et al.* [2010] using a standard averaging and fitting technique applied to plasma drift data obtained from Super Dual Auroral Radar Network (SuperDARN) coherent backscatter measurements. Convection patterns were obtained independently for the Northern Hemisphere and Southern Hemisphere, taking into account the Earth's dipole tilt angle, and it was shown that dipole tilt angle has significant impacts on the convection patterns and that not all effects were symmetric between hemispheres.

[6] In this study we seek to extend these results by modifying the binning and averaging methods, taking into account an additional interplanetary parameter that is effective in driving ionospheric convection and by adding

¹Thayer School of Engineering, Dartmouth College, Hanover, New Hampshire, USA.

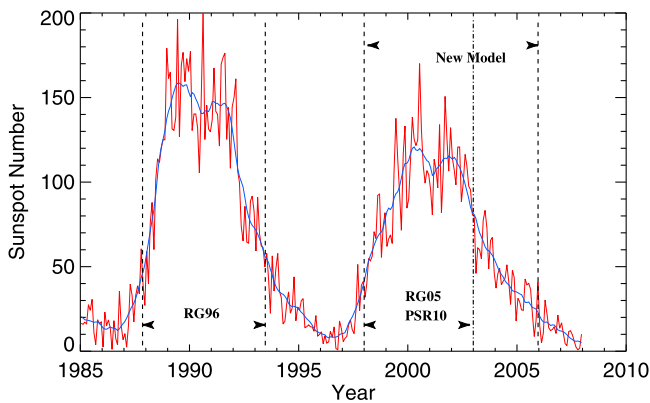


Figure 1. Monthly sunspot numbers since 1985. Time spans used in the past and current SuperDARN statistical studies are indicated with arrows.

additional functionality which allows the results to be used as a dynamical, rather than discrete, model for high-latitude convection. The improved methodology enables a better resolution of the changes in convection as the magnitude of the upstream solar wind driving conditions varies. In addition, the added dependence on the solar wind velocity gives a better representation of the strength of the driving conditions and results in statistical patterns that better reproduce the response of convection to changing interplanetary conditions. Furthermore, the use of an interpolation technique provides dynamical functionality, so that the model can produce a unique convection pattern for any given solar wind and tilt conditions within the range of the study. This functionality allows for easier comparison to data and to other models. Also, because it provides patterns which vary smoothly as the input driving conditions vary, a dynamical model is useful for operational purposes (such as constraining instantaneous SuperDARN convection patterns) and for inputting into other models. Although we deviate from the method of Pettigrew *et al.* [2010] in several significant aspects, we do, as in that study, derive independent convection patterns for the two hemispheres and for three season-like categories of dipole tilt angle (winter-like, equinox-like and summer-like conditions).

[7] The details of the methodology are described in section 2. The resulting discrete patterns of average convection, the development of the dynamical model and an example application of it are described in section 3. In section 4, we discuss how this model compares to instantaneous SuperDARN patterns of convection, to previous SuperDARN statistical convection models and to other convection models currently available in the literature.

2. Technique

[8] The technique used in this study to obtain average patterns of high-latitude convection is similar to that of Ruohoniemi and Greenwald [2005] and Pettigrew *et al.* [2010], although several significant deviations are described. These average patterns are the basis for a dynamical convection model described in section 3.2.

[9] Data for this study is obtained from the Super Dual Auroral Radar Network (SuperDARN), an international

network of ground-based high-frequency radars that measure the line-of-sight (LOS) component of the bulk $\mathbf{E} \times \mathbf{B}$ drift of ionospheric plasma in the high latitudes of both hemispheres [e.g., Greenwald *et al.*, 1995; Chisham *et al.*, 2007]. For the statistical patterns presented in this paper, all available velocity data from the nine high-latitude radars in the Northern Hemisphere and the seven radars in the Southern Hemisphere are used from January 1998 through December 2005. This time period is lengthened by three years compared to that of Ruohoniemi and Greenwald [2005] and Pettigrew *et al.* [2010] and it spans most of the last solar cycle, as shown in Figure 1. Data from later years is also available, but due to the dropoff in HF radar backscatter occurrence rates accompanying the low solar activity level [e.g., Ruohoniemi and Greenwald, 1997], including these data would give a relatively small increase in the total number of LOS measurements.

[10] One-minute resolution OMNI data are obtained from the CDAWeb database and are used to sort the velocity measurements. The OMNI data set uses multispacecraft measurements of the interplanetary parameters which are lagged to subsolar point on the Earth's bow shock [King and Papitashvili, 2005]. Values of the IMF and the solar wind velocity from the OMNI data are averaged to 10-min, nonoverlapping time bins and are further lagged from the bow shock to the magnetopause subsolar point using a standard technique, briefly described here. The lag time is calculated as $\Delta t = \Delta x / (V_x / 8)$, where Δx is the distance between the bow shock nose and the subsolar magnetopause and V_x is the antisunward component of the solar wind velocity [Lester *et al.*, 1990, 1993]. The distance Δx is determined using the subsolar locations of the bow shock, reported in the OMNI data, and the magnetopause model of Sibeck *et al.* [1991, 1992], keyed to the solar wind velocity, dynamic pressure, and magnetic field. Lag times in this study range between 2 and 7 min and are typically around 5 min, which is smaller than the 10 min binning used here. Small errors in the lag time are therefore expected to have little or no impact on the binning. In addition, a stability requirement is imposed on the IMF such that the same condition must persist at the magnetopause for at least three consecutive 10 min time bins. Furthermore, data from the first 10 min time bin are not included in order to account somewhat for errors in the lag time determination and for delay in the reconfiguration of the convection pattern [e.g., Ridley *et al.*, 1998].

[11] In previous SuperDARN statistical studies [Pettigrew *et al.*, 2010; Ruohoniemi and Greenwald, 1996, 2005, the latter two referred to hereafter as RG96 and RG05, respectively], velocity measurements are sorted into three bins based on the magnitude of the transverse component of the IMF ($B_T = \sqrt{B_y^2 + B_z^2}$, where B_y and B_z are defined in Geocentric Solar Magnetospheric, or GSM, coordinates). Data in each of these magnitude bins are further sorted into eight IMF clock angle bins. In this work, we sort the data into eight IMF clock angle bins (as before), but due to the nonuniform distribution of the IMF clock angle, in which the B_y component dominates a majority of the time, we depart slightly from the uniform spacing of the bins. Instead, we define eight IMF clock angle bins such that the bins centered at $B_z \pm$ are 50° wide, those centered at $B_y \pm$ are 40° wide and the intermediate bins are 45° wide (see Figure 2).

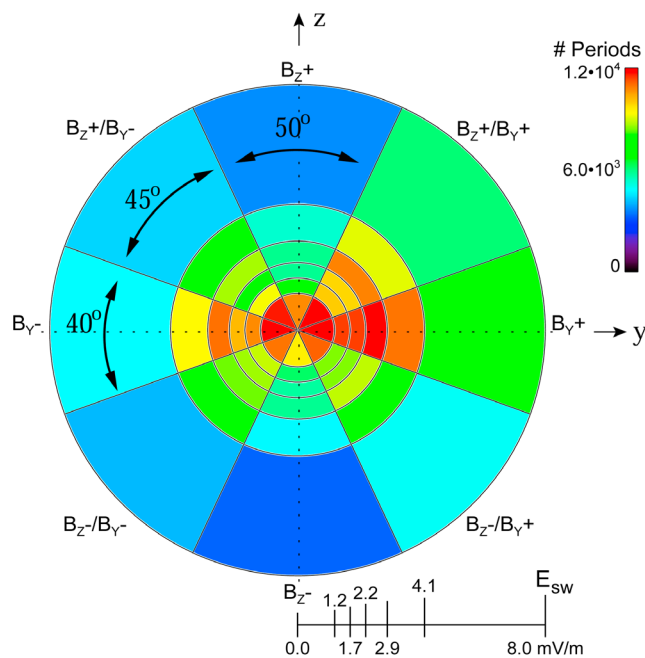


Figure 2. Statistical distribution of the IMF clock angle and E_{sw} magnitude from lagged OMNI data.

This nonuniform spacing is a subtle change from previous studies but has the advantage of giving a more uniform distribution of time periods in each clock angle bin.

[12] A more significant departure from previous studies is the introduction of a dependence on the solar wind velocity, accomplished by sorting the ionospheric velocity data by the solar wind electric field magnitude, $E_{sw} = |V_x B_T|$. Furthermore we use six, rather than three, magnitude bins that are defined by the following ranges of E_{sw} : 0–1.2, 1.2–1.7, 1.7–2.2, 2.2–2.9, 2.9–4.1, and >4.1 mV/m. The bin sizes are selected to be as narrow as possible in order to best resolve the progression of the convection pattern from weak to strong convection while still maintaining sufficient LOS measurements in each bin to fully constrain a fitted solution. The distribution of the number of time periods classified into the 48 different magnitude and clock angle bins is shown in Figure 2.

[13] The dependence on V_x is added because it has been shown to impact the strength of the coupling between the magnetosphere and ionosphere [e.g., Reiff *et al.*, 1981; Doyle and Burke, 1983]. In these studies, the observed cross-polar cap potential drop (Φ_{PC}), defined as the difference between the maximum and minimum of the high-latitude electrostatic potential distribution, is found to correlate better to empirical formulas based on solar wind parameters that include V_x than to those that do not. Using E_{sw} to sort the ionospheric velocity data can account for variations in the convection which are due to variations in the solar wind velocity while the transverse magnitude of the IMF remains constant. A similar dependence on the solar wind velocity is used in the high-latitude electric potential models of Weimer [1996, 2005]. Note that the solar wind density or ram pressure has also been shown to have an impact on convection [e.g., Boudouridis *et al.*, 2004]. However, constraints on the minimum amount of data required to derive a reliable sta-

tistical convection pattern limits the number of sorting parameters and subdivisions that can be used, and the inclusion of a density dependence is left for future work.

[14] For this study, all time periods that meet the IMF stability requirement are sorted into the IMF clock angle and E_{sw} bins described and are further sorted into three season-like categories based on dipole tilt angle according to criteria as follows. For each time period, the Earth's best fit magnetic dipole tilt angle in the GSM $x-z$ plane was calculated using the International Geomagnetic Reference Field (IGRF) model [Mandea and Macmillan, 2000]. The sign of the dipole tilt angle is reversed for Southern Hemisphere data so that in both hemispheres positive tilt is associated with sunlit conditions. This sign-modified definition of dipole tilt angle will be referred to hereafter simply as tilt. Time periods are classified as negative, neutral or positive tilt for the following ranges: tilt < -10° , $|\text{tilt}| \leq 10^\circ$ and tilt > 10° , respectively. This tilt-based classification is identical to that of Pettigrew *et al.* [2010].

[15] Having sorted all stable time periods between 1998 and 2005, any available SuperDARN LOS velocity data from these time periods are collected and tagged with their corresponding tilt, clock angle and magnitude bin information. All the LOS velocity vectors from a given IMF clock angle, E_{sw} magnitude and tilt bin are arranged onto an equal-area spatial grid with a 1° resolution in geomagnetic latitude. For each cell in this grid, all velocity vectors within the cell are sorted by their azimuthal directions into 10° wide nonoverlapping bins. The valid range of azimuthal angle magnitudes is $\leq 90^\circ$ from the pole and vectors directed away from the pole are represented with negative velocity values. The weighted mean and standard error ($SE = \sigma/\sqrt{n}$, where σ is the standard deviation) are then calculated from the vectors in each 10° azimuthal bin.

[16] Average velocities from this procedure are fit to an eighth order, eighth degree expansion of spherical harmonics according to a least squares method used in RG05 and Pettigrew *et al.* [2010]. For this method, error weighting can be specified and a lower latitude, zero potential boundary must be set. In this study, the standard error associated with each average velocity is used as an error weight. This weighting (rather than a standard deviation weighting) is selected because the standard error is an estimate of the standard deviation of the mean and therefore is a better indicator of the uncertainty in the value of the average velocity.

[17] The selection of the lower latitude limit of the spherical harmonic expansion (referred to as the Heppner-Maynard boundary, or HMB) and the use of zero padding to mimic the compressed shape of the dayside region is described by Pettigrew *et al.* [2010] and is also used in this study. The electrostatic potential distribution implied by the fitted velocities can then be calculated using the equations $\mathbf{V} = (\mathbf{E} \times \mathbf{B})/B^2$, $\mathbf{E} = -\nabla\Phi$, with \mathbf{B} calculated at each velocity's location using the IGRF model.

[18] Because there is generally much less HF radar backscatter during summer conditions when the high latitudes are completely sunlit [e.g., Ruohoniemi and Greenwald, 1997], it is necessary to modify somewhat the sorting bins for the positive tilt patterns. The modifications described here ensure that each bin contains sufficient LOS measurements across the entire high-latitude region in order to fully constrain the fitted solution and thus fully define the derived convection

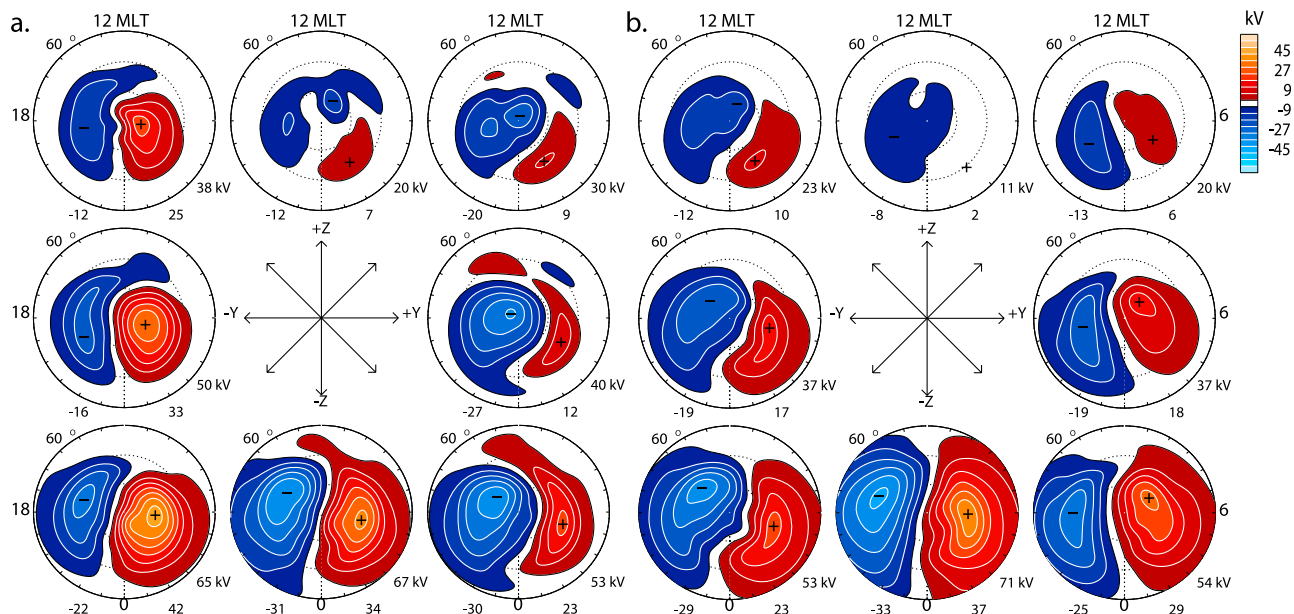


Figure 3. Average convection patterns for $2.2 < E_{sw} < 2.9$ mV/m, sorted by IMF clock angle. (a) Northern Hemisphere patterns for tilt $> 10^\circ$. (b) Southern Hemisphere patterns for tilt $< -10^\circ$. IMF direction is indicated by arrows at the center of each panel. The low-latitude limit of each plot is 60° , and the patterns are rotated such that noon MLT is at top and 6 MLT is at right. Electrostatic potential is indicated by color according to the scale at top right, and equipotential contours are shown at 6 kV increments. The locations of the potential maxima (plus signs) and minima (minus signs) are marked, and their values in kV are shown at bottom right and left, respectively. The cross-polar cap potential difference is given at lower right of each plot.

pattern. In the Southern Hemisphere, velocity data from the lowest two E_{sw} magnitude bins are merged and data from the middle two bins are merged such that there are four, rather than six, magnitude bins for positive tilt, corresponding to: 0–1.7, 1.7–2.9, 2.9–4.1, and >4.1 mV/m. Additionally, the highest magnitude bin for positive tilt conditions in the Southern Hemisphere is expanded to include all time periods with tilt $>5^\circ$. The remaining two tilt bins are left unmodified. This slight modification to the tilt binning provides enough additional data to constrain the patterns without further compromising the magnitude resolution and it has only a small impact on the ability to resolve tilt-dependent changes in the convection. In the Northern Hemisphere, the lowest two E_{sw} magnitude bins are merged to create one larger bin spanning 0–1.7 mV/m, while the remaining four magnitude bins and all tilt bins are left unchanged. Due to these modifications, the progression of the convection pattern with increasing E_{sw} is less well-resolved for positive tilt conditions than it is for neutral and negative tilt conditions, but these minor changes ensure sufficient data coverage in all patterns without losing any refinement in the patterns for neutral and negative tilt.

3. Results

3.1. Discrete Patterns of Convection

[19] Using the technique described in section 2, we obtain 127 and 119 independent convection patterns for the Northern Hemisphere and Southern Hemisphere, respectively. A representative set of northern and Southern Hemisphere patterns is shown in Figure 3 for positive tilt in

the north, negative tilt in the south (such as would occur during northern summer) and moderate driving strength ($2.2 < E_{sw} < 2.9$ mV/m, e.g., IMF $B_T = 5$ nT, $V_x = 500$ km/s).

[20] Although it will be shown that these patterns differ from those of RG05 and Pettigrew *et al.* [2010] in their response to changes in the strength of the solar wind driving conditions, they do exhibit IMF clock angle and tilt dependencies similar to those of prior models. These dependencies are briefly described here.

[21] In both hemispheres, as the IMF clock angle approaches B_z^- (southward IMF) the magnitudes of the flows increase and the value of Φ_{PC} increases. As the IMF goes from B_z dominated to B_y dominated, both the dayside and nightside of the convection pattern rotate clockwise in MLT for positive (negative) B_y and counterclockwise in MLT for negative (positive) B_y in the north (south). The dawn and dusk convection cells are shaped into round and crescent cells, with the round cell located at dusk in the north (south) under positive (negative) IMF B_y and at dawn under negative (positive) IMF B_y .

[22] As tilt progresses from negative to positive in both hemispheres, reverse convection that increases in magnitude is seen in the IMF B_z^+ patterns while little change is seen in the B_z^- patterns. For increasing tilt under IMF B_y dominated conditions, the shaping into round and crescent cells and the rotation in MLT is reinforced for IMF B_{y^+} (B_{y^-}) in the north (south) but weakened for IMF B_{y^-} (B_{y^+}) in the north (south). In both hemispheres, flows in the round cell are enhanced with increasing tilt, especially under IMF B_{y^-} . IMF B_y and tilt dependencies of statistical convection patterns are discussed in more detail by Pettigrew *et al.* [2010].

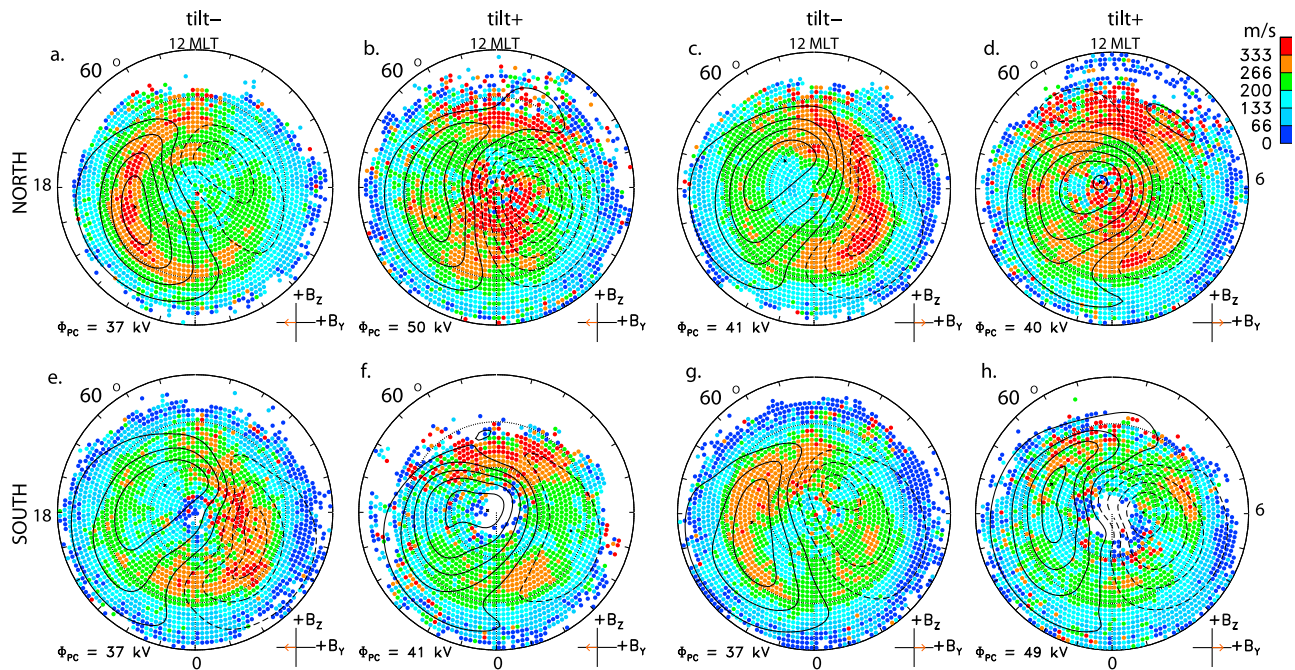


Figure 4. Maps of model variability for $2.2 < E_{sw} < 2.9$ mV/m. Color indicates standard deviation in m/s, according to the color scale at top right, and electrostatic potential contours are overlaid at 6 kV intervals. IMF magnitude and direction are indicated by an arrow at the bottom right of each map.

[23] In addition to producing average patterns of large-scale convection in the high-latitude regions, the analysis described in section 2 also provides information on the amount of variation in the velocity data going into each pattern. Note that the temporal and spatial variability in local flow velocities during a given contiguous time period (with stable IMF) contributes only a fraction of the total amount of variation seen in the velocities in this statistical study. A large component of the total variability is the variations between flow velocities taken at the same geomagnetic location but from different time periods. These variations are likely due to differences in driving conditions or preconditioning that are not accounted for in the model parameters [cf. *Cosgrove and Codrescu, 2009*]. Distinguishing the two sources of velocity variability is of interest but is beyond the scope of this paper and left to future work. The total amount of variation within a given spatial grid cell will be referred to hereafter as the model variability. It is also important to note that this model variability does not account for any variations in velocity that occur on timescales or spatial scales smaller than the resolution of the model.

[24] The model variability is obtained at each grid cell by calculating the standard deviations of the LOS velocity measurements in each azimuthal direction (see section 2) and taking a weighted average of the values from all directions, giving one scalar variability value for each cell. Increased model variability is observed in areas with strong velocity shears, such as at the convection reversal boundaries [cf. *Shepherd et al., 2003*], in areas with enhanced flow magnitudes and in areas which contain relatively high numbers of LOS velocity measurements.

[25] Figure 4 shows the model variability in both hemispheres for IMF $B_y \pm$, tilt \pm for the 2.2–2.9 mV/m magnitude

bin (as in Figure 3). Under negative tilt with IMF $B_y \pm$ (Figures 4a, 4c, 4e, and 4g), bands of large variability (with magnitudes up to 400 m/s) are seen along the center of the crescent-shaped convection cells where the sharpest convection reversal boundaries occur (at dawn in Figures 4a and 4g and dusk in Figures 4c and 4e). Under positive tilt (Figures 4b, 4d, 4f, and 4h), when convection in the round cell tends to be enhanced, less variability is seen in the crescent cell and more (magnitudes up to 400 m/s) is seen across the high-latitude polar cap where the flow magnitudes tend to be large. These variability magnitudes are of the same order of magnitude as the average velocity values, which are approximately 600 m/s across the polar cap and in the return flow below the convection reversal boundaries. Model variability also tends to increase in the cusp region, which has previously been observed to be a highly variable region [e.g., *Matsuo et al., 2003*]. As discussed by *Pettigrew et al. [2010]*, the ability of the model to predict instantaneous flow velocities is decreased in regions where the model variability is large, due to the lack of consistency in the velocities observed in these regions.

[26] The spherical harmonic coefficients for the convection patterns shown in Figure 3 and the data for model variability maps shown in Figure 4, as well as those for the remaining tilt and solar wind conditions (not shown here), are available from the author and can be obtained at the following URL: <http://engineering.dartmouth.edu/superdarn>.

3.2. A Dynamical Model of Convection

[27] In past studies, average convection patterns have been used as a set of discrete patterns, represented by a set of coefficients of a spherical harmonic expansion, for finite ranges (bins) of B_T or E_{sw} , IMF clock angle, and tilt angle. It

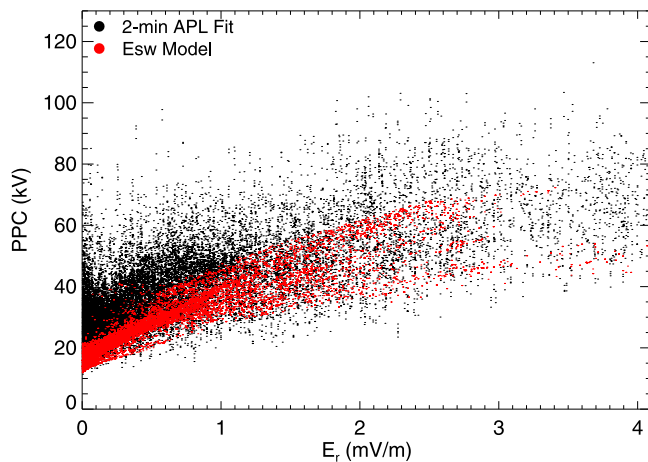


Figure 5. Values of Φ_{PC} for the Northern Hemisphere from the instantaneous APL FIT patterns of March 2002 and values from the interpolated model patterns for the instantaneous solar wind conditions.

is possible, however, to infer intermediate patterns by performing a trilinear interpolation through these coefficients. The discrete model coefficients are assumed to apply at the midpoints of the parameter bins. Between the midpoints of two neighboring bins, the coefficients are assumed to have a linear dependence on the three parameters, tilt angle, E_{sw} magnitude and $\sin(\theta/2)$, where θ is the IMF clock angle. Linear interpolation is used to determine intermediate values for the coefficients based on the difference between the specified values of the parameters and the midpoints of the parameter bins. A simple linear interpolation is possible because the coefficients vary roughly linearly across the various bins. It is found that interpolating for coefficients at a point halfway between two bin midpoints results in a pattern with a value of Φ_{PC} equal to the average of the Φ_{PC} values of the two bins, consistent with the assumption of linearity. This technique allows the average convection patterns to form the basis for a dynamical model that is capable of producing a high-latitude convection pattern for any IMF and solar wind conditions that are within the parameter ranges used to determine the discrete patterns.

[28] One important consideration in determining the ranges over which this dynamical model is valid is that under the largest driving conditions ($E_{sw} > 4.1$ mV/m, $B_z < 0$), the convection pattern expands to lower latitudes that are, in fact, equatorward of the field of view of the radars. As a result, there are not sufficient data to fully define average patterns for B_z^- or B_z^-/B_y^\pm in the largest magnitude bin for any of the three tilt categories and these patterns are omitted from the discrete model presented here. Without a basis of average patterns and without extrapolation it is not possible to run the dynamical model for IMF clock angles between 90° (B_y^+) and 270° (B_y^-) if the E_{sw} magnitude is greater than 4.1 mV/m.

[29] One possible application of this dynamical model is in calculating Φ_{PC} values for specified driving conditions, without requiring any instantaneous ionospheric velocity data. To demonstrate this application and compare its results to primarily data-driven results, we select an equinoctial

month that includes a wide variety of solar wind driving conditions and generally large occurrence rates of SuperDARN backscatter and apply the following procedure. For each 2 min time period in March 2002 with lagged IMF data available from OMNI, the standard operational spherical harmonic fitting procedure (APL FIT) is applied to the instantaneous SuperDARN LOS data to determine a global convection pattern and measure the Φ_{PC} [Ruohoniemi and Baker, 1998; Shepherd and Ruohoniemi, 2000]. The interpolation technique is then used to determine a model convection pattern for the solar wind conditions which prevail at that time.

[30] The Φ_{PC} values determined by the data and by the model are plotted in Figure 5 against the reconnection electric field E_r , defined as $E_r = V_x B_T \sin^2(\theta/2) = E_{sw} \sin^2(\theta/2)$. For $E_r < 3$ mV/m, the growth of Φ_{PC} with E_{sw} is approximately linear for both the model and data values.

[31] Note that no stability criteria were imposed on the IMF so estimating the proper lag time to propagate the solar wind conditions to the ionosphere is more critical and any errors add uncertainty to the values of E_r for each of the 2 min time periods. The large spread in the instantaneous Φ_{PC} values for low E_r is likely due to errors in this lag time calculation and due to the finite time required for the reconfiguration of the convection pattern [e.g., Ridley *et al.*, 1998], both of which could be significant compared to the 2 min time resolution. The effect of the variable IMF and finite reconfiguration time accompanied by errors in propagating the solar wind conditions is likely to be more pronounced at lower values of E_r due to relatively more variability in the weakly driven convection compared to that observed under strongly driven convection. Even across the entire range of E_r , however, there is a large spread in the instantaneous values of Φ_{PC} . The uncertainty in the value E_r is likely to be a source of some of the variations in Φ_{PC} . The variations could also be due in part to clock angle dependencies that are not accounted for by the $\sin^2(\theta/2)$ term (such as asymmetric responses to positive and negative IMF B_y) and due in part to dipole tilt angle dependencies [e.g., Pettigrew *et al.*, 2010]. These clock angle and tilt effects are captured by the statistical model and the model shows a similar spread in the values of Φ_{PC} . The model, however, does not account for all the interplanetary parameters which might affect convection, such as solar wind density, and it does not account for any preconditioning of the M-I system [e.g., Wygant *et al.*, 1983]. As a result, somewhat greater variability is seen in the data-determined values of Φ_{PC} than in the model-determined values.

[32] The magnitudes of the model Φ_{PC} are similar to those of the instantaneous Φ_{PC} , other than for low values of E_r when the effective driving conditions of the instantaneous patterns are less certain. For $1 < E_r < 3$ mV/m, the average percent difference between the model- and data-derived Φ_{PC} values is -7.5% . Above $E_r = 3$ mV/m, both the model and data values of Φ_{PC} appear to level off somewhat. This does not necessarily point to a saturation of the convection, though, because at this level of driving conditions the convection patterns expand below the field of view of the radars, making a definitive measure of Φ_{PC} difficult. For driving conditions with $E_r \approx 4$ mV/m or greater and IMF $B_z < 0$, it is not possible to accurately measure Φ_{PC} using

the spherical harmonic fitting procedure with the high-latitude radars as the only data source. In the future, inclusion of data from another source with midlatitude coverage, such as midlatitude SuperDARN radars, could be used to expand the range of driving conditions over which this measurement technique is valid.

[33] The dynamical model described is also available from the author and at the URL: <http://engineering.dartmouth.edu/superdarn>.

4. Discussion

[34] To put the model presented here in context, we compare it with well-defined instantaneous SuperDARN convection patterns, with the results of previous SuperDARN statistical studies, and with other models of high-latitude convection based on other data sets and techniques.

[35] We begin with a brief discussion of possible sources and magnitudes of uncertainty in the model, for the purpose of better understanding which differences are likely to be significant and which are not.

4.1. Model Uncertainty

[36] To obtain a rough estimate of the uncertainty introduced to the model by variations in the velocity data, the LOS data from one magnitude bin were randomly divided into two subsets and each subset was binned by IMF clock angle and tilt and was averaged and fitted to an expansion of spherical harmonics, following the technique described in section 2. The average convection patterns obtained from each subset were compared to the original pattern (derived from all the data) by comparing both the values of Φ_{PC} and the RMS difference between the electrostatic potential distributions.

[37] In both Northern and Southern Hemisphere, the differences in Φ_{PC} are less than 6 kV for all tilt angles and all IMF clock angles and are less than 3 kV (10%) for most conditions. The median difference in Φ_{PC} between the original convection pattern and the patterns derived from subsets of the data is 0.6 kV (1.4%) in the north and 0.5 kV (1.5%) in the south. The differences are greatest for positive tilt and for IMF B_z^- , when there is less data constraining the solutions, and the subsequent decimation required by this uncertainty estimation technique further reduces the completeness of data coverage. In these cases, we expect that this technique overestimates the uncertainty that is present in patterns obtained using the complete data set.

[38] In both hemispheres, the RMS differences between the electrostatic potential distributions are less than 2.5 kV for $B_z \geq 0$ and range from 2 to 6 kV for $B_z < 0$. The median RMS difference is 1.5 kV (1.2 kV) for $B_z \geq 0$ and 4 kV (3 kV) for $B_z < 0$ in the north (south).

[39] Errors and uncertainties are also introduced by the averaging and fitting technique. In particular, we investigate the effect of the selection of the azimuthal angle bin size, which influences how many LOS measurements are averaged together before they are input to the fitting procedure, and the selection of the lower latitude limits of the fitted solutions (the HMB). For every convection pattern (all tilts, all magnitudes and all IMF clock angles), a fitted solution was calculated with the HMB set at $\pm 2^\circ$ from the original, and for azimuthal bin sizes of 15° , 20° and 30° (the original

is 10°). For each pattern, the standard deviation (σ) of the six different values of Φ_{PC} (the original and five variations), was calculated. In both hemispheres, σ increases with increasing values of Φ_{PC} , ranging from approximately 0 kV to 2 kV (corresponding to $\sim 3\%$) in the north and 0 kV to 4 kV ($\sim 5\%$) in the south. The larger variations in Φ_{PC} in the Southern Hemisphere are probably due to the smaller number of original LOS velocity measurements.

[40] When making comparisons among patterns produced by the model presented in this work, differences of 10% (roughly twice the upper estimate of model uncertainty) or more will be considered significant. This threshold will also be used when making comparisons with other works because estimates of the uncertainty in the other models are not available.

4.2. Comparison With Instantaneous SuperDARN Convection Patterns

[41] To demonstrate that the changes seen in the large-scale convection features of the model as the tilt and IMF clock angle vary are indeed representative of features seen in real time, we compare the output of the dynamical model with a selection of instantaneous convection patterns derived using SuperDARN data from individual time periods.

[42] For this comparison, we select eight 10 min time periods for which IMF $|B_y| \gg |B_z|$, the dipole tilt is either large and positive or large and negative and there are sufficient instantaneous SuperDARN LOS measurements that the convection pattern is well defined in one hemisphere. For these time periods, the APL FIT procedure is used to obtain instantaneous, global convection patterns that are then compared to the model output for the specified solar wind and tilt conditions.

[43] Figure 6 shows eight time periods for IMF $B_y \pm$, tilt \pm in the Northern Hemisphere and Southern Hemisphere. The instantaneous SuperDARN patterns are shown in Figures 6a, 6b, 6c, and 6d for the north and Figures 6i, 6j, 6k, and 6l for the south. The corresponding interpolated model patterns are shown in Figures 6e, 6f, 6g, and 6h and Figures 6m, 6n, 6o, and 6p for the north and south respectively. In all the patterns, electrostatic potential contours are shown at 6 kV intervals and velocity vectors are shown with both length and color indicating magnitude; the same velocity color scale is used in both the instantaneous and model plots. Note that there are fewer radars operating in the south than in the north during these time periods and therefore the Southern Hemisphere instantaneous convection patterns are not as well constrained as those in the Northern Hemisphere. There is therefore a corresponding lower confidence in the instantaneous measure of Φ_{PC} in the south than in the north.

[44] During negative tilt (winter-like) periods, the Northern Hemisphere and Southern Hemisphere instantaneous patterns are very similar to each other if the comparison is made under opposite signs of IMF B_y . Comparing, for example, Figures 6a to 6k or 6c to 6i shows no significant differences in the morphology of the flows. The values of Φ_{PC} for these patterns do, however, differ, partly due to differences in the driving conditions but most likely due to transients in the convection that are not reproduced identically during different time periods even though the driving conditions are similar. The model patterns for negative tilt

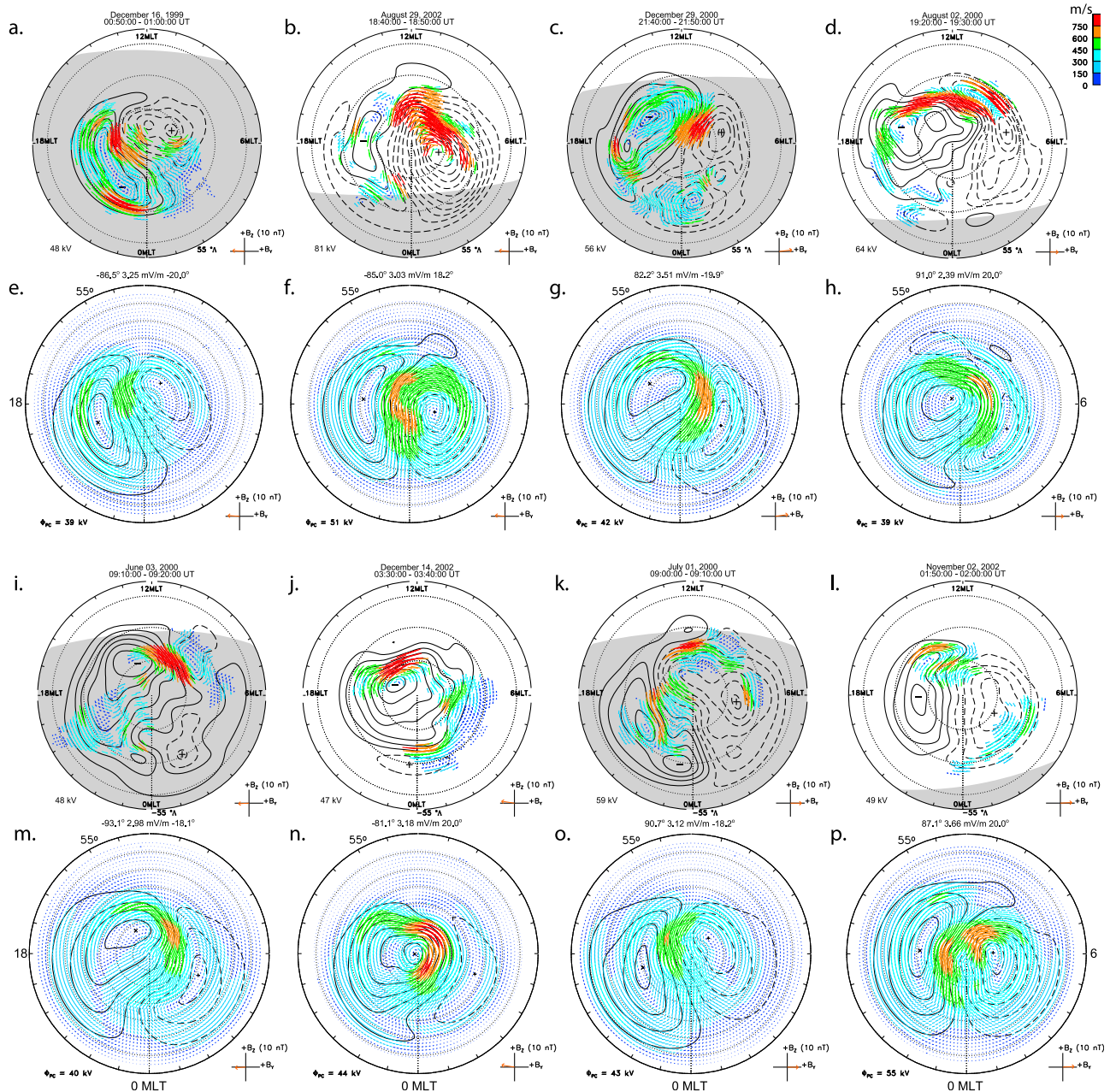


Figure 6. Instantaneous SuperDARN convection maps for the Northern Hemisphere and Southern Hemisphere for 10 min time periods with IMF $B_y\pm$, tilt \pm . Model patterns are shown immediately below the corresponding instantaneous patterns (see text for details). The date and time are given above each instantaneous map, and the prevailing IMF clock angle, E_{SW} magnitude, and tilt are indicated above each model pattern. In all patterns, electrostatic potential contours are shown at 6 kV intervals, and velocity vectors are shown with both length and color indicating magnitude. (top right) The velocity color scale is used in both the instantaneous and model plots. (bottom right) IMF magnitude and direction are indicated by an arrow in each map. (bottom left) Φ_{PC} values are given in each map.

(Figures 6e and 6o or Figures 6g and 6m) also show this interhemispheric symmetry.

[45] During positive tilt (summer-like) periods, the instantaneous patterns exhibit the same tilt effects that are seen in the average patterns (described in section 3). Under IMF B_y- in both hemispheres (Figures 6b and 6j), convection primarily occurs in the round cell, which is significantly

enhanced both in size and flow magnitudes as compared to the negative tilt patterns (Figures 6a and 6i). Under IMF B_y- (B_y+) in the north (south), the counterclockwise rotation that is typically seen during negative or neutral tilt periods (e.g., Figures 6a and 6k), is not seen in the positive tilt periods (Figures 6b and 6l). Under IMF B_y+ (B_y-) in the north (south), the typical shaping into round and crescent

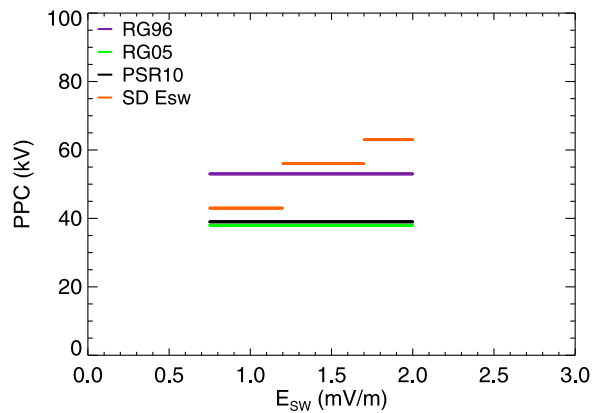


Figure 7. Values of Φ_{PC} for the Northern Hemisphere from the statistical models of RG96, RG05, *Pettigrew et al.* [2010] (PSR10), and the current model (SD Esw). The IMF clock angle and transverse magnitude B_T are fixed at 180° (B_z^-) and 2.5 nT, respectively, while the solar wind velocity is varied over 300–800 km/s.

cells with a dominate round dusk cell (e.g., Figures 6c and 6i) is reinforced under positive tilt (Figures 6d and 6j).

[46] These asymmetric effects of tilt and IMF B_y imply that the instantaneous convection patterns can be very different between the northern and Southern Hemisphere if the dipole tilt is nonzero and the IMF is B_y dominated, as is shown to be the case in average patterns by *Pettigrew et al.* [2010] and in this study. For instance, at a given point in time when the Earth’s dipole tilt is positive, the Northern Hemisphere has a positive tilt and the Southern Hemisphere a negative tilt. If the IMF B_y is negative, this corresponds to Figures 6d and 6i. In these examples, though the magnitudes of E_{sw} and the IMF clock angle differ by just 0.05 mV/m and 8° , respectively, the flow configurations are very different between the hemispheres, with the southern (winter) hemisphere exhibiting a typical two cell pattern with enhanced flows very localized to the cusp region while the Northern (summer) Hemisphere shows a very dominant dawn cell with enhanced flows extending from the cusp toward the dayside and the dawn flank. Furthermore, the values of Φ_{PC} differ by $\sim 70\%$. These differences are reproduced in the model patterns (Figures 6f and 6m), although the difference in the values of Φ_{PC} is not as extreme.

[47] For all eight examples shown in Figure 6, the model patterns reproduce most of the mesoscale features present in the instantaneous patterns. The greatest discrepancy is in the values of Φ_{PC} , where the model values of Φ_{PC} are generally much smaller (by $\sim 30\%$ on average) than those of the instantaneous patterns. This difference could be due in part to the selection processes for the case study: selecting times with the most backscatter might tend to favor times when the convection is more enhanced than what is seen on average for a given driving condition. The model potential values are also likely to be attenuated somewhat by the significant amount of filtering and averaging that is required to produce the statistical patterns. This filtering and averaging, when applied to the highly variable velocity data (as discussed in section 3.1), tends to smooth out large velocity shears, reducing potential drops.

[48] Despite having somewhat lower potentials than instantaneous patterns, the model patterns do reproduce the instantaneous flow configurations and the relative differences in convection strengths between different cells in one pattern or between the same pattern under different tilts. They also accurately indicate which region (e.g., cusp, polar cap, flank, dawnside, duskside) will contain large-magnitude flows.

4.3. Comparison to Previous SuperDARN Statistical Models

[49] To illustrate the effect of introducing a solar wind velocity dependence to the model and of the modification to the binning technique, we compare it to previous SuperDARN statistical models [RG96; RG05; *Pettigrew et al.*, 2010]. To better match these models, which provided discrete sets of convection patterns, the dynamical functionality described in section 3.2 will not be used for the following comparison. A simple and convenient but far from comprehensive method for comparing the models is to look at differences in their values of Φ_{PC} .

[50] The Φ_{PC} values of all the average convection patterns derived in this study are generally higher (by approximately 10% on average) than those of RG05 and *Pettigrew et al.* [2010] for the same driving conditions, assuming an average solar wind velocity of 450 km/s applied to the previous models. This difference is not large, but is probably significant as discussed in section 4.1. A likely cause of this difference is the additional sorting by the solar wind velocity and the smaller magnitude bins used in this study, which results in less averaging together of LOS velocity data from widely varying driving conditions that would tend to attenuate larger velocity values.

[51] A representative comparison of the different SuperDARN statistical models for variable solar wind velocity is shown in Figure 7, which shows the values of Φ_{PC} from each model for $B_z = -2.5$ nT, $B_y = 0$ nT and neutral tilt with the solar wind velocity ranging from 300 to 800 km/s. These conditions span three of the E_{sw} magnitude bins of the model presented here (SD Esw model) and the value of Φ_{PC} increases with solar wind velocity as expected. The models of RG96, RG05, and *Pettigrew et al.* [2010] (referred to as PSR10) did not take into account solar wind velocity, and therefore these conditions are all classified under the same magnitude range and the values of Φ_{PC} remain constant. Note that the value of Φ_{PC} from the RG96 model is approximately equal to the average of the three values of the current model, possibly because it was based on data from just one radar and thus used less data reduction and averaging than did the models RG05 and *Pettigrew et al.* [2010].

4.4. Comparison to Other Models

[52] Finally, we demonstrate how the model presented here compares with other models derived from other data sets using differing techniques. As in section 4.3, we use differences in the values of Φ_{PC} as a simple and convenient method of measuring differences between the various models. For this comparison, we consider the statistical patterns of *Haaland et al.* [2007] and *Förster et al.* [2007], based on Cluster Electron Drift Instrument (EDI) electric field measurements mapped to the high-latitude ionosphere (EDI model); those of *Papitashvili and Rich* [2002], based on DMSP ion drift measurements at 840 km (DCIM model);

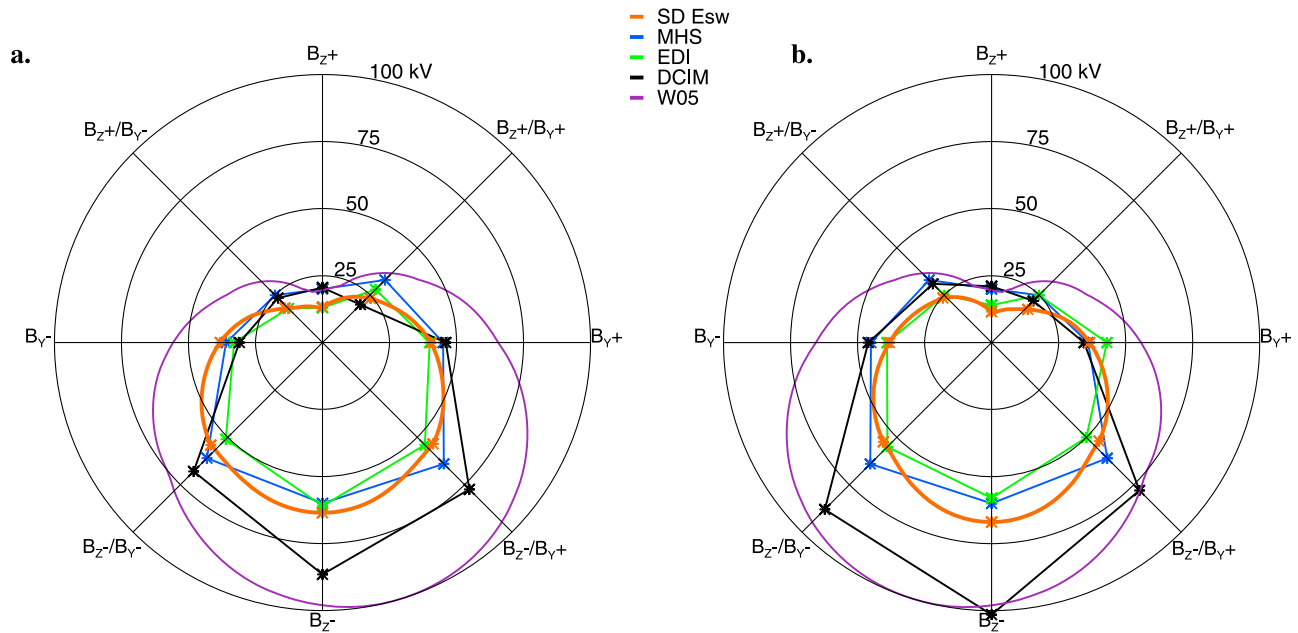


Figure 8. Φ_{PC} values from various models for (a) the Northern Hemisphere and (b) the Southern Hemisphere plotted against IMF clock angle (see text for details).

those of *Zhang et al.* [2007], based on Millstone Hill and Sondrestrom incoherent scatter radar velocity measurements (MHS model); and those of *Weimer* [2005], based on Dynamics Explorer 2 electric field measurements at 300–1000 km (W05 model). For all these models, Φ_{PC} values are obtained for as similar of conditions as possible. The conditions for which the various models are applicable and the method used to obtain from these models values of Φ_{PC} which best correspond to each other are briefly described here.

[53] The EDI model is given as a set of average convection patterns for the Northern Hemisphere and Southern Hemisphere, based on all available EDI data from February 2001 to March 2006, sorted by IMF clock angle but independent of IMF B_T , solar wind velocity or season. The median IMF B_T and solar wind velocity were approximately 5.3 nT and 430 km/s, respectively, and the median tilt was slightly negative [*Haaland et al.*, 2007; *Förster et al.*, 2007]. Because this model uses the fewest sorting parameters, patterns from the remaining models will be selected to best match the median solar wind and tilt conditions of the EDI study.

[54] The DCIM model provides convection patterns for both hemispheres for winter, equinox and summer for IMF $B_T = 5$ nT and unspecified solar wind velocities [*Papitashvili and Rich*, 2002, Figures 2–4]. The Φ_{PC} values from the winter and equinox patterns were averaged together to best approximate the EDI model conditions. The slight difference in the magnitude of IMF B_T is unavoidable.

[55] The MHS statistical patterns shown in Figure 2 of *Zhang et al.* [2007] are independent of season and are given for IMF $B_y = (-4,0,4)$ nT and $B_z = (-4,0,4)$ nT and unspecified solar wind velocity. Values of Φ_{PC} are taken directly from these patterns. Due to the variation in the magnitude of IMF B_T for the different IMF clock angles,

these patterns are the hardest to compare directly to those of the remaining models.

[56] Because the W05 model and the model derived in this study (SD Esw model) are both dynamical models, the values of Φ_{PC} from these models are simply calculated for IMF $B_T = 5.3$ nT, $V_{sw} = 430$ km/s ($E_{sw} = 2.3$ mV/m) and tilt = -10° .

[57] Figure 8 shows the Φ_{PC} values of the various models plotted in polar format for varying IMF clock angles, similar to the format introduced by *Haaland et al.* [2007]. Note that the MHS and W05 models only provide convection patterns for the Northern Hemisphere, so for these models the northern Φ_{PC} values are assumed to apply in the Southern Hemisphere with the sign of IMF B_y reversed.

[58] Even though the conditions are not identical, the values of Φ_{PC} from the MHS, EDI and the SuperDARN model of this study are all very similar to each other for all IMF clock angles. For IMF $B_z \geq 0$, the DCIM values are also similar to the values from these models, but the DCIM values are much larger for IMF $B_z < 0$. Values of Φ_{PC} calculated from the W05 model are on average 50% larger than those of the model derived in this study. Values from this study and from the EDI model, on the other hand, fall within 5%–15% of one another.

[59] A large component of the spread in the Φ_{PC} values from the three models that are similar to each other is likely due to differences in the driving conditions. It remains unclear, however, why Φ_{PC} values from the W05 model and from the DCIM model for IMF $B_z < 0$ are significantly larger than those of the other three models. These differences could be due in part to a difference in the latitude coverage of the instrument sets. The ground based radar and Cluster EDI data sets have little or no data available below approximately 60° geomagnetic latitude, while the low-altitude satellite studies have no latitude limitations and

include data down to approximately 50° geomagnetic latitude. The convection potential contribution from these latitudes, however, is expected to be small at the moderate driving conditions used for this comparison, because at this driving level the convection pattern has not expanded below 60° .

[60] Another possible source of differences in the models' values of Φ_{PC} is the IMF stability requirements and the degree of averaging used in deriving the models. The SuperDARN model presented here and the Cluster EDI model (the two most similar models) both impose a 30 min stability requirement on the IMF and both apply spatial binning and averaging to the velocity values. The W05 model (which is most different from the remaining models) does not impose an IMF stability requirement and does not apply spatial binning and averaging. These differences in technique are likely to affect the resulting average convection patterns and their values of Φ_{PC} . The IMF stability requirement might allow the convection pattern to stabilize to some degree and the spatial binning and averaging of large numbers of measurements is expected to smooth out large shears in the velocity data, likely reducing the electrostatic potential differences.

5. Summary

[61] In this study, we have derived a dynamical model that specifies the high-latitude convection electrostatic potential distribution in the Northern or Southern Hemisphere for any dipole tilt and for any IMF and solar wind conditions that are within the parameter ranges covered by the underlying data. This dynamical model is based on discrete average convection patterns derived from high-latitude plasma flow data from SuperDARN measurements collected over eight years of the past solar cycle. The analytical technique used in this study is a modification of that used by RG05 and Pettigrew *et al.* [2010]. More specifically, the technique of those studies is improved by, among other modifications, increasing the number of magnitude bins, thus increasing the resolution of the model with changing solar wind driving strength, and by introducing a dependence on the solar wind velocity to account for variations in the convection pattern that are driven by changes in the solar wind velocity while the magnitude of IMF B_T remains constant.

[62] The discrete, average convection patterns derived here exhibit IMF clock angle and dipole tilt dependencies that are consistent with those observed by Pettigrew *et al.* [2010]. The model variability associated with these discrete patterns is also calculated and is seen to increase in areas with strong velocity shears, such as at the convection reversals, in areas with enhanced flow magnitudes, and in areas which contain relatively high numbers of original LOS velocity measurements. As a result, spatial maps of model variability are found to exhibit IMF clock angle and dipole tilt dependencies.

[63] Both the dynamical model of this study and instantaneous SuperDARN global convection patterns have Φ_{PC} values that grow approximately linearly with E_r for weak and moderate values of that parameter, the range over which this model is valid. For a given value of E_r , however, the model shows significant variations in the value of Φ_{PC} , similar to the variations in the instantaneously calculated

Φ_{PC} . The variations in the model values of Φ_{PC} are the result of IMF clock angle and dipole tilt dependencies that are not accounted for in the parameter E_r but have been shown to affect convection. These effects are likely to account for some of the variation seen in the instantaneous values of Φ_{PC} as well.

[64] It is also demonstrated that the statistical model developed in this study reproduces the mesoscale features of high-latitude convection that are seen in instantaneous SuperDARN convection patterns. Although model values of Φ_{PC} are lower than the corresponding instantaneous values for the time periods selected, relative differences between convection patterns from different IMF clock angles and/or tilts are reproduced. In addition, Φ_{PC} values from this model are found to be larger than those of RG05 and Pettigrew *et al.* [2010] but similar to several other data-derived models of high-latitude convection that are currently available in the literature.

[65] Although the current lack of data equatorward of the locations of the ground-based high-latitude SuperDARN radars limits the dynamic range of this model to $E_{sw} < 4.1$ mV/m when IMF $B_z < 0$, within this range the model can be used for operational purposes (such as constraining instantaneous SuperDARN convection patterns) and for specifying the high-latitude electric field distribution in other models which require knowledge of its state.

[66] **Acknowledgments.** Operation of the SuperDARN radars is supported by the national funding agencies of the United States, Canada, the United Kingdom, France, Japan, Italy, South Africa, and Australia. We gratefully acknowledge the CDAWeb for providing the high-resolution OMNI data used in this study. This work was supported by NSF grants ATM-0836485 and ATM-0838356 and NASA grant NNG-05667H.

[67] Robert Lysak thanks Raymond Greenwald and another reviewer for their assistance in evaluating this paper.

References

- Boudouridis, A., E. Zesta, L. R. Lyons, and P. C. Anderson (2004), Evaluation of the Hill-Siscoe transpolar potential saturation model during a solar wind dynamic pressure pulse, *Geophys. Res. Lett.*, *31*, L23802, doi:10.1029/2004GL021252.
- Chisham, G., et al. (2007), A decade of the Super Dual Auroral Radar Network (SuperDARN): Scientific achievements, new techniques and future directions, *Surv. Geophys.*, *28*, 33–109.
- Cosgrove, R. B., and M. V. Codrescu (2009), Electric field variability and model uncertainty: A classification of source terms in estimating the squared electric field from an electric field model, *J. Geophys. Res.*, *114*, A06301, doi:10.1029/2008JA013929.
- Cowley, S. W. H. (1982), The causes of convection in the Earth's magnetosphere: A review of developments during the IMS, *Rev. Geophys.*, *20*, 531–565, doi:10.1029/RG020i003p00531.
- Cowley, S. W. H., and M. Lockwood (1992), Excitation and decay of solar wind-driven flows in the magnetosphere-ionosphere system, *Ann. Geophys.*, *10*, 103–115.
- Doyle, M. A., and W. J. Burke (1983), S3-2 measurements of the polar cap potential, *J. Geophys. Res.*, *88*, 9125–9133, doi:10.1029/JA088iA11p09125.
- Dungey, J. W. (1961), Interplanetary magnetic field and the auroral zones, *Phys. Rev. Lett.*, *6*, 47–48.
- Förster, M., G. Paschmann, S. E. Haaland, J. M. Quinn, R. B. Torbert, H. Vaith, and C. A. Kletzing (2007), High-latitude plasma convection from cluster EDI: Variances and solar wind correlations, *Ann. Geophys.*, *25*, 1691–1707.
- Foster, J. C., J. M. Holt, R. G. Musgrove, and D. S. Evans (1986), Ionospheric convection associated with discrete levels of particle precipitation, *Geophys. Res. Lett.*, *13*, 656–659, doi:10.1029/GL013i007p00656.
- Greenwald, R. A., et al. (1995), DARN/SuperDARN: A global view of the dynamics of high-latitude convection, *Space Sci. Rev.*, *71*, 761–796.

- Haaland, S. E., G. Paschmann, M. Förster, J. M. Quinn, R. B. Torbert, C. E. McIlwain, H. Vaith, P. A. Puhl-Quinn, and C. A. Kletzing (2007), High-latitude plasma convection from cluster EDI measurements: Method and IMF dependence, *Ann. Geophys.*, *25*, 239–253.
- Heppner, J. P., and N. C. Maynard (1987), Empirical high-latitude electric field models, *J. Geophys. Res.*, *92*, 4467–4489, doi:10.1029/JA092iA05p04467.
- Holt, J. M., R. H. Wand, J. V. Evans, and W. L. Oliver (1987), Empirical models for the plasma convection at high latitudes from Millstone Hill observations, *J. Geophys. Res.*, *92*, 203–212, doi:10.1029/JA092iA01p00203.
- King, J. H., and N. E. Papitashvili (2005), Solar wind spatial scales in and comparisons of hourly wind and ace plasma and magnetic field data, *J. Geophys. Res.*, *110*, A02104, doi:10.1029/2004JA010649.
- Lester, M., M. P. Freeman, D. J. Southwood, J. A. Waldock, and H. J. Singer (1990), A study of the relationship between interplanetary parameters and large displacements of the nightside polar cap boundary, *J. Geophys. Res.*, *95*, 21,133–21,145, doi:10.1029/JA095iA12p21133.
- Lester, M., O. de la Beaujardière, J. C. Foster, M. P. Freeman, H. Lühr, J. M. Ruohoniemi, and W. Swider (1993), The response of the large scale ionospheric convection pattern to changes in the IMF and substorms: Results from the SUNDIAL 1987 campaign, *Ann. Geophys.*, *11*, 556–571.
- Lester, M., S. E. Milan, G. Provan, and J. A. Wild (2006), Review of ionospheric effects of solar wind magnetosphere coupling in the context of the expanding contracting polar cap boundary model, *Space Sci. Rev.*, *124*, 117–130.
- Lu, G., P. H. Reiff, M. R. Hairston, R. A. Heelis, and J. L. Karty (1989), Distribution of convection potential around the polar cap boundary as a function of the interplanetary magnetic field, *J. Geophys. Res.*, *94*, 13,447–13,461, doi:10.1029/JA094iA10p13447.
- Mandea, M., and S. Macmillan (2000), International Geomagnetic Reference Field—The eighth generation, *Earth Planets Space*, *52*, 1119–1124.
- Matsuo, T., A. D. Richmond, and K. Hensel (2003), High-latitude ionospheric electric field variability and electric potential derived from DE-2 plasma drift measurements: Dependence on IMF and dipole tilt, *J. Geophys. Res.*, *108*(A1), 1005, doi:10.1029/2002JA009429.
- Papitashvili, V. O., and F. J. Rich (2002), High-latitude ionospheric convection models derived from Defense Meteorological Satellite Program ion drift observations and parameterized by the interplanetary magnetic field strength and direction, *J. Geophys. Res.*, *107*(A8), 1198, doi:10.1029/2001JA000264.
- Papitashvili, V. O., B. A. Belov, D. S. Faermark, Y. I. Feldstein, S. A. Golyshv, L. I. Gromova, and A. E. Levitin (1994), Electric potential patterns in the northern and southern polar regions parameterized by the interplanetary magnetic field, *J. Geophys. Res.*, *99*, 13,251–13,262, doi:10.1029/94JA00822.
- Papitashvili, V. O., F. J. Rich, M. A. Heinemann, and M. R. Hairston (1999), Parameterization of the Defense Meteorological Satellite Program ionospheric electrostatic potentials by the interplanetary magnetic field strength and direction, *J. Geophys. Res.*, *104*, 177–184, doi:10.1029/1998JA900053.
- Pettigrew, E. D., S. G. Shepherd, and J. M. Ruohoniemi (2010), Climatological patterns of high-latitude convection in the Northern and Southern hemispheres: Dipole tilt dependencies and interhemispheric comparisons, *J. Geophys. Res.*, *115*, A07305, doi:10.1029/2009JA014956.
- Reiff, P. H., and J. L. Burch (1985), IMF B_y -dependent plasma flow and Birkeland currents in the dayside magnetosphere: 2. A global model for northward and southward IMF, *J. Geophys. Res.*, *90*, 1595–1609, doi:10.1029/JA090iA02p01595.
- Reiff, P. H., R. W. Spiro, and T. W. Hill (1981), Dependence of polar cap potential drop on interplanetary parameters, *J. Geophys. Res.*, *86*, 7639–7648, doi:10.1029/JA086iA09p07639.
- Ridley, A. J., G. Lu, C. R. Clauer, and V. O. Papitashvili (1998), A statistical study of the ionospheric convection response to changing interplanetary magnetic field conditions using the assimilative mapping of ionospheric electrodynamic technique, *J. Geophys. Res.*, *103*, 4023–4039, doi:10.1029/97JA03328.
- Ruohoniemi, J. M., and K. B. Baker (1998), Large-scale imaging of high-latitude plasma convection with Super Dual Auroral Radar Network HF radar observations, *J. Geophys. Res.*, *103*, 20,797–20,811, doi:10.1029/98JA01288.
- Ruohoniemi, J. M., and R. A. Greenwald (1996), Statistical patterns of high-latitude convection obtained from Goose Bay HF radar observations, *J. Geophys. Res.*, *101*, 21,743–21,763, doi:10.1029/96JA01584.
- Ruohoniemi, J. M., and R. A. Greenwald (1997), Rates of scattering occurrence in routine HF radar observations during solar cycle maximum, *Radio Sci.*, *32*(3), 1051–1070, doi:10.1029/97RS00116.
- Ruohoniemi, J. M., and R. A. Greenwald (2005), Dependencies of high-latitude plasma convection: Consideration of interplanetary magnetic field, seasonal, and universal time factors in statistical patterns, *J. Geophys. Res.*, *110*, A09204, doi:10.1029/2004JA010815.
- Ruohoniemi, J. M., S. G. Shepherd, and R. A. Greenwald (2002), The response of the high-latitude ionosphere to IMF variations, *J. Atmos. Sol. Terr. Phys.*, *64*(2), 159–171.
- Shepherd, S. G., and J. M. Ruohoniemi (2000), Electrostatic potential patterns in the high latitude ionosphere constrained by SuperDARN measurements, *J. Geophys. Res.*, *105*, 23,005–23,014, doi:10.1029/2000JA000171.
- Shepherd, S. G., J. M. Ruohoniemi, and R. A. Greenwald (2003), Direct measurements of the ionospheric convection variability near the cusp/throat, *Geophys. Res. Lett.*, *30*(21), 2109, doi:10.1029/2003GL017668.
- Sibeck, D. G., R. E. Lopez, and E. C. Roelof (1991), Solar wind control of the magnetopause shape, location, and motion, *J. Geophys. Res.*, *96*, 5489–5495, doi:10.1029/90JA02464.
- Sibeck, D. G., R. E. Lopez, and E. C. Roelof (1992), Reply, *J. Geophys. Res.*, *97*, 10,879–10,882, doi:10.1029/92JA00141.
- Weimer, D. R. (1995), Models of high-latitude electric potentials derived with a least error fit of spherical harmonic functions, *J. Geophys. Res.*, *100*, 19,595–19,607, doi:10.1029/95JA01755.
- Weimer, D. R. (1996), A flexible, IMF dependent model of high-latitude electric potentials having “space weather” applications, *Geophys. Res. Lett.*, *23*, 2549–2552, doi:10.1029/96GL02255.
- Weimer, D. R. (2001), An improved model of ionospheric electric potentials including perturbations and application to the Geospace Environment Modeling November 24, 1996, event, *J. Geophys. Res.*, *106*, 407–416, doi:10.1029/2000JA000604.
- Weimer, D. R. (2005), Improved ionospheric electrodynamic models and application to calculating Joule heating rates, *J. Geophys. Res.*, *110*, A05306, doi:10.1029/2004JA010884.
- Wygant, J. R., R. B. Torbert, and F. S. Mozer (1983), Comparison of S3-3 polar cap potential drops with the interplanetary magnetic field and models of magnetopause reconnection, *J. Geophys. Res.*, *88*, 5727–5735, doi:10.1029/JA088iA07p05727.
- Zhang, S.-R., J. M. Holt, and M. McCready (2007), High latitude convection based on long-term incoherent scatter radar observations in North America, *J. Atmos. Sol. Terr. Phys.*, *69*, 1273–1291.

E. D. P. Cousins and S. G. Shepherd, Thayer School of Engineering, Dartmouth College, Hanover, NH 03755, USA. (ellen.cousins@dartmouth.edu)